



1 **Formaldehyde and Glyoxal Measurement Deploying a Selected**
2 **Ion Flow Tube Mass Spectrometer (SIFT-MS)**

3

4 Antonia G. Zogka, Manolis N. Romanias,* and Frederic Thevenet

5 ¹ IMT Nord Europe, Institut Mines-Télécom, Univ. Lille, CERI EE, F-59000 Lille, France

6 *Correspondence to:* Manolis N. Romanias (emmanouil.romanias@imt-nord-europe.fr)

7

8

9



10 **Abstract.** Formaldehyde (FM) and glyoxal (GL) are important atmospheric species of indoor and outdoor
11 environments. They are either directly emitted in the atmosphere or they are formed through the oxidation of organic
12 compounds by indoor and/or outdoor atmospheric oxidants. Despite their importance, the real-time monitoring of
13 these compounds with soft ionization mass spectrometric techniques, e.g. proton transfer mass spectrometry (PTR-
14 MS), remains problematic and is accompanied by low sensitivity. In this study, we evaluate the performance of a
15 multi-ion selected ion flow tube mass spectrometer (SIFT-MS) to monitor in real-time atmospherically relevant
16 concentrations of FM and GL under controlled experimental conditions. The SIFT-MS used is operated under standard
17 conditions (SC), as proposed by the supplier, and custom conditions (CC), to achieve higher sensitivity. In the case of
18 FM, SIFT-MS sensitivity is marginally impacted by RH, and the detection limits achieved are below 200 ppt.
19 Contrariwise, in the case of GL, a sharp decrease of instrument sensitivity is observed with increasing RH when the
20 H_3O^+ ion is used. Nevertheless, the detection of GL using NO^+ precursor ion is moderately impacted by moisture with
21 an actual positive sensitivity response. Therefore, we recommend the use of NO^+ precursor for reliable detection and
22 quantitation of GL. This work evidences that SIFT-MS can be considered as an efficient tool to monitor the
23 concentration of FM and GL using SIFT-MS in laboratory experiments and potentially in indoor or outdoor
24 environments. Furthermore, SIFT-MS technology still allows great possibilities for sensitivity improvement and high
25 potential for monitoring low proton transfer affinity compounds.

26
27 **Keywords:** SIFT-MS; PTR-MS; Formaldehyde; Glyoxal; H_3O^+ ; NO^+ ; charge transfer reaction;
28 quantification.
29



30 1. Introduction

31 Formaldehyde (CH₂O, FM) is the lightest aldehyde. It is a ubiquitous chemical compound in outdoor and
32 indoor environments. FM is a toxic and carcinogenic air contaminant with adverse health effects to humans
33 (Bernstein et al., 1984; Kim et al., 2011). In the open atmosphere, formaldehyde is mainly formed by the
34 oxidation of volatile organic compounds (VOCs), (Kefauver et al., 2014). Fuel combustion, forest fires and
35 agricultural activities are also important sources of FM outdoors (Kaiser et al., 2015; Lee et al., 1997;
36 Luecken et al., 2012). FM plays an important role in atmospheric photochemistry since it is photolysed,
37 producing hydroxyl (OH) and hydroperoxy (HO₂) radicals which drive ozone (O₃) production, (Atkinson,
38 2000). Thus, it enhances the formation of secondary organic aerosol (SOA) (Li et al., 2011). In indoor
39 environments, FM can be emitted directly from wood-based materials, construction materials, paintings,
40 anthropogenic activities such as smoking, cooking, cleaning, or by the oxidation of indoor VOCs, especially
41 terpenes, with high yields (Salthammer, 2019). Indoor concentrations of FM can reach significantly higher
42 levels than outdoors (Crump et al., 1997; Langer et al., 2015; Liu et al., 2006).

43
44 Glyoxal (C₂H₂O₂, GL) is the lightest α -dicarbonyl compound. GL has been identified as precursor of
45 secondary organic aerosol (SOA) outdoors (Fu et al., 2008; Liggio et al., 2005; Volkamer et al., 2007;
46 Rossignol et al., 2014). GL is formed in the atmosphere by the oxidation of biogenic and anthropogenic
47 VOCs, such as isoprene (the highest emitted VOC in the atmosphere), and acetylene (Fu et al., 2008; Xiao
48 et al., 2007; Myriokefalitakis et al., 2008). The oxidation of aromatic compounds in the presence of NO_x
49 (NO, NO₂) also produces GL. Other sources of GL are biomass burning, fossil and biofuel combustion,
50 (Grosjean et al., 2001; Hays et al., 2002; Kean et al., 2001) as well as oceans, but literature studies report a
51 high variability (Mahajan et al., 2014; Sinreich et al., 2010). In literature it has also been reported that the
52 photochemical oxidation of glyoxal in the troposphere leads to HO_x radical formations (Salter et al., 2013).
53 In indoor environments, to the best of our knowledge, there are no studies reporting the direct emission or
54 secondary formation of glyoxal, but, considering emerging research activities dealing with indoor air
55 quality, this should not be excluded.

56
57 Due to their important role in the chemistry of outdoor and indoor environments, the monitoring of the FM
58 and GL in laboratory experiments (e.g. simulation chamber experiments, photochemical reactors) or in field
59 (indoor and outdoor) is of significant importance in order to evaluate and understand the underlying
60 chemistry. Nevertheless, the real time measurement of FM and GL is not a trivial process. The sensitivity
61 of the classically used proton transfer mass spectrometry (PTR-MS) technique for these compounds is quite
62 limited and is strongly impacted by relative humidity (Inomata et al., 2008; Stönnner et al., 2017; Vlasenko
63 et al., 2010; Yuan et al., 2017). Limitations are mainly due to the low proton transfer affinities (PA) of both
64 compounds of interest : $PA_{FM} = 713 \text{ kJ mol}^{-1}$ and $PA_{GL} = 675\text{-}690 \text{ kJ mol}^{-1}$ (Wróblewski et al., 2007), and
65 thus very close to the PA of water, $PA_{H_2O} = 691 \text{ kJ mol}^{-1}$. Quite recently, electron attachment reaction
66 (EAR) ionization mass spectrometry has been used for real-time measurements of GL in ambient air.
67 Nevertheless, this technique does not seem to be sensitive enough for other volatile organic compounds
68 (VOCs) (Lu et al., 2019). It should be noted that mass spectrometric techniques are widely applied in
69 atmospheric science for three main reasons. First, they are sensitive tools, able to monitor simultaneously
70 and in real-time a wide range of VOCs. Second, they are robust, user-friendly and mobile systems. Third,
71 they require a relatively low sampling flow (in the order of hundred $\text{cm}^3 \text{ min}^{-1}$) and can be easily coupled
72 to “small scale” laboratory experiments or with other instrumentation without a significant extra demand
73 on air sampling flow.



74

75 Alternatively, the monitoring of FM and GL is achieved using VOC-selective spectroscopic techniques
76 such as Fourier transform infrared spectroscopy (FTIR) (Catoire et al., 2012), differential optical absorption
77 spectroscopy (DOAS) (Coburn et al., 2014), tunable-diode laser absorption spectrometer (TDLAS) (Catoire
78 et al., 2012), or incoherent broadband cavity-enhanced absorption spectrometer (IBBCEAS) (Liu et al.,
79 2019; Lu et al., 2019). FTIR spectroscopy is mostly used in lab experiments (Catoire et al., 2012) deployed
80 in-situ or in line configuration inside atmospheric simulation chambers or photoreactors (Wisthaler et al.,
81 2008). However, the sensitivity is relatively poor and even long optical path FTIR systems achieve detection
82 limits (DL) in the order of several parts per billion (ppb). In addition, long path FTIR systems are not
83 mobile, or of limited mobility, and the selective detection of FM and GL is relatively difficult due to the
84 complex IR pattern in the presence of other VOCs. Other VOC-selective spectroscopic tools such as DOAS
85 and IBBCEAS, are mostly used in outdoor field studies (Coburn et al., 2014; Lu et al., 2019). These are
86 expensive and delicate systems that can achieve detection limits in the sub-ppb level. However, these
87 techniques require a high volume sampling flow of several liters per minute (L min^{-1}) (Coburn et al., 2014;
88 Lu et al., 2019). Thus, they are not commonly deployed in laboratory studies or indoor field measurements.
89 Therefore, low time resolution techniques such as off-line analytical approaches are used for the selective
90 determination of FM and GL. In particular gas chromatography and mass spectrometry (GC-MS), or high-
91 performance liquid chromatography (HPLC) are used for off line analysis of sampling cartridges (Ban-
92 Weiss et al., 2008; Gómez Alvarez et al., 2012; Wisthaler et al., 2008).

93

94 A response to the need for real-time, selective and sensitive monitoring of FM and GL could be the selected
95 multi-ion flow tube mass spectrometry (SIFT-MS). SIFT-MS is a soft ionization analytical technique,
96 mainly used for the real time monitoring (identification and quantification) of a wide diversity of VOCs,
97 and some inorganic species (e.g. NO_2 , HONO). SIFT-MS attains the advantages of typical mass
98 spectrometric techniques described above. SIFT-MS is essentially a double quadrupole chemical ionization
99 mass spectrometer using simultaneously H_3O^+ , NO^+ , and O_2^+ precursor ions for the ionization and the
100 subsequent detection of the analytes. SIFT-MS has extensively been used for breath analysis, and in food
101 science, but it is not commonly used in atmospheric science, where traditionally, PTR-MS is widely applied.
102 Nevertheless, in the last decade, the application of SIFT-MS technology for the study of atmospheric
103 relevant processes became more frequent, where SIFT-MS is either coupled to experimental chambers with
104 various volumes for indoor studies (Caron et al., 2016; Caron et al., 2020; Thevenet et al., 2021), or
105 atmospheric simulation chambers for the study of VOC degradation (Osseiran et al., 2020; Allani et al.,
106 2021).

107

108 Quite recently, Lacko et al. (2020) have reported for the first time the detection of FM and GL deploying a
109 custom made SIFT-MS. In their study, authors mainly focus on the ion chemistry occurring inside the flow
110 tube of the instrument and how it is impacted by humidity. These authors have also applied chemical
111 modeling in an attempt to interpret their experimental results. Nevertheless, Lacko et al. (2020) used a
112 custom-made SIFT-MS instrumentation that was operated in a tailored mode, injecting the corresponding
113 VOC in a humidified air flow of helium bath gas. Their measurements were carried out at low levels of
114 relative humidity, never exceeding 10 %, and using constant concentrations of VOCs in the ppm range.
115 Therefore, authors did not evaluate the response of the instrument in a VOC concentration span of sub-ppm
116 range, typical of indoor and outdoor environments, and they did not report the corresponding detection
117 limits (DL). Furthermore, their study was solely focused on the chemistry of H_3O^+ precursor ion.



118

119 In this paper, we present a series of calibration experiments of FM and GL deploying a commercially
120 available SIFT-MS Voice 200 Ultra instrument. The main objective of this work is to evaluate the
121 sensitivity of SIFT-MS towards FM and GL, and elucidate whether it can (i) be used to monitor the
122 concentrations of the title compound in laboratory scale or ambient indoor / outdoor air conditions and (ii)
123 overcome the limitations encountered in conventional PTR-MS studies as highlighted above. In addition,
124 for the first time in literature, we aim to emphasize the importance of NO^+ charge transfer reactions on the
125 detection of GL. To meet these objectives, FM and GL calibration measurements are carried out under
126 dynamic flow conditions using a wide range of VOC concentrations in the ppb level, varying the relative
127 humidity (RH) from dry to 70 %. Within that framework we assess the impact of RH and the instrument
128 operational conditions (i.e. pressure and temperature) to its performance.

129

130 The structure of the article is as follows: first we present a detailed description of the experimental set up,
131 the methods deployed and protocols followed in this work. Thereafter, in the results and discussion section
132 we provide (i) literature and experimental evidences that impact charge transfer reactions in SIFT-MS and
133 PTR-MS, and (ii) the actions made in the framework of our study to improve SIFT-MS performance.
134 Subsequently, results and discussion on FM and GL are presented separately in two different sections. Each
135 of the two subsections include the presentation of our experimental observation, and a thorough discussion
136 that contains (i) comparison with PTR-MS or other SIFT-MS studies, and (ii) comprehensive assessment
137 of the charge transfer reactions involved in the detection of the compound of interest.

138

139 2. Experimental Section

140 2.1 Materials

141 **Formaldehyde source.** A gas cylinder of formaldehyde purchased from praxair (12 ppm in N_2) is used as
142 a source for the calibration experiments. The purity and stability of the gas mixture is regularly tested by
143 sampling formaldehyde gas on DNPH cartridges (Waters) eluted and analyzed off-line using UltiMate 3000
144 HPLC instrument (Thermo Scientific) coupled with an ultraviolet detector.

145 **Glyoxal source.** The monomer of pure glyoxal is synthesized applying a similar method with the literature
146 (Volkamer et al., 2005). In particular, equal amounts (ca. 0.6 g) of glyoxal trimer dihydrate (purity ≥ 97 %
147 Sigma-Aldrich) and di-phosphorous pentoxide (purity > 98 %, VWR Chemicals) are mixed in a glass bulb
148 and are progressively heated up under vacuum (1.5×10^{-3} Torr) from room temperature to 453 K. The
149 evolving gas is collected in a glass trap immersed into liquid nitrogen where the bright yellow pure GL
150 solid crystals appear. Subsequently, after synthesis, the cold trap containing the monomer of GL is placed
151 in a liquid nitrogen/ethanol bath maintained at 230 K, and is degassed under vacuum several times to
152 remove volatile by-products (purification process). The vapors of pure GL are collected in a 10 L Pyrex
153 glass bulb, darkened to minimize exposure of the sample to room light. The purity of the gas is verified by
154 FTIR spectroscopy deploying an Antaris FTIR spectrophotometer equipped with a 2 L optical gas cell with
155 10 m optical path length. The temperature of the optical cell is maintained at 353 K. The FTIR spectra
156 collected are of high quality and identical to those presented in literature for pure GL monomers (Volkamer
157 et al., 2005). The thermal stability of the GL is also verified, and we evidence that no thermal decomposition
158 occurs, in accordance with the literature (Feierabend et al., 2008; Saito et al., 1984). Considering the
159 detection limits of the instrument for CO, CO_2 (in the order of 0.1 ppm), and formaldehyde (in the order of
160 1 ppm, the purity of GL is greater than 99 %. After the quality control experiments, dilutions of GL gas in



161 He are prepared manometrically in another glass bulb, with mixing ratios of ca. 1 % for a total pressure of
162 400 Torr. For the sake of simplicity it will be referred to as mixture 1 (GL diluted in He) in the following.
163 Mixture 1 is used as a source to prepare more diluted GL/He gas mixtures (in the range of 50 to 120 ppm)
164 with total pressure of 1550 Torr inside a 6 L silonite treated canister. The exact concentration of GL in the
165 canister is determined with FTIR spectroscopy using the well-defined broad band IR absorption cross
166 section coefficients provided in literature for the characteristic band of GL between 2724-2940 cm^{-1}
167 (Volkamer et al., 2005). These mixtures are used for the calibration of the SIFT-MS instrument and their
168 stability is evaluated on a daily basis. It should be noted that two different GL syntheses have been carried
169 out and 4 different GL+He canister mixtures are used for the calibration experiments to evaluate
170 uncertainties related to GL concentration.

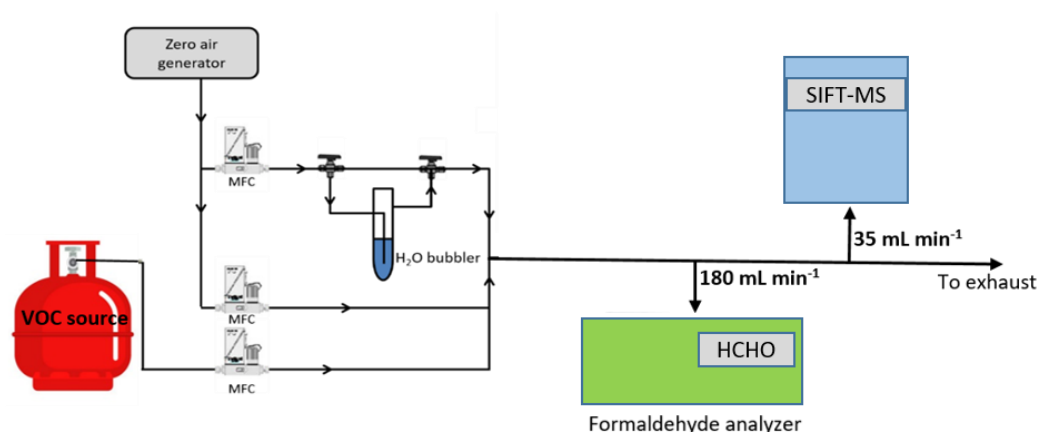
171

172 2.2 Experimental Setup

173

174 General Description

175 The experimental set up used in the current study is reported in Fig. 1. The gas flow generation lines are
176 made of Teflon. Calibrated mass flow controllers (MFC) are used to mix the flow of the target VOC (i.e.
177 FM or GL) with dry or humid zero air (impurity levels: VOCs < 0.1 ppb, CO_2 < 10 ppb, and CO < 80 ppb,
178 moisture level: ca. 2 ppm). The total gas flow rates in the calibration measurements are in the order of 1000
179 mL min^{-1} . Nevertheless, experiments are also performed varying the flow rate between 300 to 1600
180 mL min^{-1} aiming to evaluate the possible loss of compounds on gas lines. The total concentration of the target
181 VOCs in the diluted gas flow are between 40 to 1200 ppb. In the case of FM, the diluted gas stream is
182 sampled by an ap2e ProCeas formaldehyde analyzer (sampling rate 180 mL min^{-1}) and the SIFT-MS
183 (sampling rate 35 mL min^{-1}) connected in parallel. Concerning GL calibration experiments, the
184 formaldehyde analyzer and the long path FTIR were occasionally used to evaluate possible impurities in
185 the canister or transformation of GL in the gas lines, but the majority of the measurements are carried out
186 by-passing them.



187



188 **Figure 1.** Experimental set-up used in the framework of the current study.

189

190 **Formaldehyde analyzer ap2e ProCeas**

191 The real time measurement of FM in the gas flow is achieved deploying an ap2e ProCeas gas analyzer. The
192 gas flow is sampled through a sonic orifice with a diameter of few micrometers. Then, the gas is driven to
193 an optical cell and analyzed employing patented laser optical feedback cavity enhanced absorption infrared
194 spectroscopy. The instrument response is ca. 2 seconds and the detection limit (3σ) of FM is 1ppb for an
195 integration time of 1 minute.

196

197 **SIFT-MS**

198 The SIFT-MS voice 200 ultra (Syft technology) is a double quadrupole chemical ionization mass
199 spectrometer. A microwave discharge generates simultaneously three precursor ions, H_3O^+ , NO^+ and O_2^+ ,
200 which are sequentially selected by a first quadrupole mass filter (Smith and Španěl, 2005). Then, under a
201 flow of He, used as carrier gas, the precursor ions are driven inside a low pressure flow tube reactor. At the
202 same time, the sampling flow is injected at the upstream-end of the reactor. The precursor ions react with
203 the analytes along the flow tube to form characteristic ionized molecules as reaction products (Smith and
204 Španěl, 2005). The temperature of the sampling port and the flow tube are regulated to avoid contaminations
205 of the sampling line and adsorption of reactants along the flow tube. Subsequently, the gas stream passes
206 through a skimmer, located at the downstream end of the flow tube reactor, and finally is injected in a high
207 vacuum chamber where both the precursor and reaction product-ions are focused, via electrostatic lenses,
208 into a second quadrupole for mass analysis and ion counting. At this point it should be noted that the
209 simultaneous presence of the three precursor ions allows the real-time monitoring of several VOCs
210 eliminating the effect of mass peak overlapping due to the use of a quadrupole mass filter with a low mass
211 resolution. Interestingly, this multi-ion chemistry allows SIFT-MS to discriminate isobaric compounds
212 (Guimbaud et al., 2007), which is not a trivial task even for time of flight (TOF) techniques (Stönnner et al.,
213 2017; Yuan et al., 2017).

214

215 **2.3 Experimental Procedure and Detection Limits**

216

217 Figure 2 displays the experimental strategy followed in the framework of the current study to calibrate the
218 SIFT-MS. In a typical calibration experiment, initially the background of the VOC of interest is monitored
219 for at least 20 min under a stream of zero air at the selected RH. Then the desired level of VOC is introduced
220 in the gas stream and its concentration is monitored in real time. In each calibration step the flows are kept
221 constant for around 20 min. In case of FM, the stabilization of its concentration in the gas flow is achieved
222 within the first 10 min after its introduction in the gas flow while in case of GL, its concentration is
223 stabilized almost instantaneously. Typically 4 to 6 different concentration levels of the VOC of interest are
224 set in each calibration experiment. At the end, the background is recorded again. This experimental
225 procedure is repeated for each level of RH and for each VOC individually. In the case of FM the calibration
226 factor is determined by plotting the SIFT-MS response (in counts) versus the concentration reported by the
227 FM analyzer; while in the case of GL by plotting the SIFT-MS response as a function of GL concentration
228 determined by the measured flow rate and the sample mixing ratio.

229



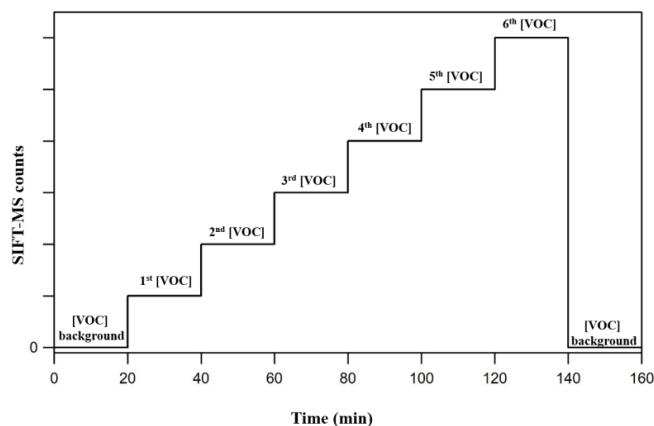
230 The time resolution of the SIFT-MS instrument in the calibration experiments is set to 1 second. FM is
231 monitored at the mass peak $m/z = 31$ (CH_3O^+ , FM- H^+) arising from H_3O^+ precursor ion, while in the case
232 of GL the mass peaks $m/z = 59$ ($\text{C}_2\text{H}_3\text{O}_2^+$) and $m/z = 88$ ($\text{C}_2\text{H}_2\text{O}_2\cdot\text{NO}^+$), originating from H_3O^+ and NO^+
233 respectively are used.

234 To determine the detection limits (DL) of the SIFT-MS Eq. (1) is used:

$$235 \quad DL = \frac{3.3 \times SD}{\text{calibration factor}} \quad \text{Eq. (1)}$$

236 where SD is the standard deviation of the background signal. Similar criterion has been used in literature to
237 determine the detection limits of PTR-MS instruments for FM and GL. Therefore, it will allow to make a
238 direct comparison between the instrument sensitivities.

239



240

Figure 2. Strategy followed during a typical calibration experiment. At first, the background of the VOC at the corresponding mass peak(s) is recorded. Then its concentration is progressively increased and monitored with SIFT-MS. Typically, 4 to 6 different concentrations of the VOC of interest are set before returning to background monitoring.

241 **3. Results and Discussion**

242 Results and discussion section is divided in three parts. In the first one, we discuss the optimization of
243 operational parameters and conditions of the SIFT-MS and the strategy followed to improve the method
244 and the performance of the instrument. The second and the third subsections are dedicated to the calibration
245 measurements of FM and GL respectively, as a function of RH under standard and custom SIFT-MS
246 operational conditions.

247

248 **3.1 From Standard to Custom Method for SIFT-MS Determination of FM** 249 **and GL**

250 The standard operational conditions (SC) of the SIFT-MS, as recommended by the supplier, correspond to:
251 (i) temperature of 393 K for the sampling plate and the flow tube, (ii) He flow rate of 380 mL min^{-1} as bath
252 gas, (iii) sampling flow rate of 35 mL min^{-1} , resulting in a total pressure inside the flow tube of 0.65 Torr



253 (Table 1). Table 1 summarizes other characteristic parameters of the SIFT-MS such as carrier gas (v_g) and
254 ions flow (v_i) velocities, reaction time inside the flow tube of the instrument (t_r), mean kinetic energy
255 between reactants (KE_{cm}). However, literature studies have reported that FM and GL detection is highly
256 sensitive to operational conditions of soft ionization mass spectrometers (Lacko et al., 2020; Stönnner et al.,
257 2017; Yuan et al., 2017). In particular, the detection of FM and GL is based on association reactions, (Lacko
258 et al., 2020; Michel et al., 2005; Stönnner et al., 2017; Yuan et al., 2017) and thus the pressure and
259 temperature of the flow tube can play a dominant role since association reactions are favored at higher
260 pressures. Furthermore, in literature the fragmentation of GL has been reported, leading to reduced
261 sensitivity and a more complex chemistry inside the reaction tube of the corresponding mass spectrometer
262 (Lacko et al., 2020; Stönnner et al., 2017). Crucial role for the detection of both FM and GL is also played
263 by the KE_{cm} (Hansel et al., 1997).

264

265 Considering the abovementioned challenges related to the sensitive detection of FM and GL, to improve
266 the sensitivity of the SIFT-MS we modified the pressure and temperature conditions of the SIFT-MS
267 compared with SC. In particular, we indirectly increased the pressure inside the flow tube, by increasing
268 He flow to its maximum value of 500 mL min^{-1} , under constant pumping. This increase in He flow results
269 in a 23 % higher pressure compared with SC. The temperature of the flow tube and sampling plate has been
270 decreased to 323K. The temperature decrease results in lower KE_{cm} . Combined with increasing pressure, it
271 leads to lower gas and ion flow velocities, and longer reaction times in the flow tube. Based on the literature
272 (as described below, experimentally validated in our study), these modifications are anticipated to increase
273 the sensitivity of the instrument. These modified operation conditions of the SIFT-MS are summarized in
274 Table 1. In the following of the manuscript, they are referred to as custom conditions (CC). In order to
275 assess the relevance of CC, calibration experiments described in the following of the manuscript are carried
276 out under both SC and CC conditions.

277

278 **Table 1.** SIFT-MS parameters and conditions used in the framework of the current study.

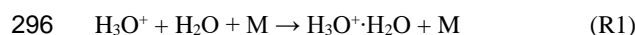
Parameters	Standard operation conditions (SC)	Custom operation conditions (CC)
Flow tube length, ^a L (cm)	34	
Flow tube internal diameter, D (cm)	4.1	
Sample plate temperature (K)	393	323
Flow tube temperature, T_g (K)	393	323
Flow tube pressure (Torr)	0.65	0.85
Molecular density in the flow tube, N (molecule cm^{-3})	1.6×10^{16}	2.5×10^{16}
Carrier gas flow (mL min^{-1})	380	500
Carrier gas flow rate, F_g (Torr L s^{-1})	5.12	6.69



Carrier gas flow velocity, ^b v_g (cm s ⁻¹)	860	705
Ion flow velocity, ^c v_i (cm s ⁻¹)	1290	1058
Reaction time, ^d t_r (ms)	27.5	33.5
Mean kinetic energy between reactants, ^e KE_{cm} (eV)	0.05	0.04
H ₂ O concentration range injected in the flow tube, ^f (molecule cm ⁻³)	(0.01-943)×10 ¹²	(0.02-1160)×10 ¹²
FM concentration range injected in the flow tube, ^g (molecule cm ⁻³)	(0.68-13.6)×10 ⁸	(0.83-16.6)×10 ⁸
GL concentration range injected in the flow tube, ^g (molecule cm ⁻³)	(0.68-16.9)×10 ⁸	(0.83-20.0)×10 ⁸

279 ^a: Distance between sample flow injection point and the end of the flow tube; ^b: calculated from the expression $v_g =$
 280 $\frac{4F_g T_g}{P_g \pi D^2 273}$ where F_g is the carrier gas flow rate, T_g the temperature of the carrier gas, P_g the pressure in flow tube, and
 281 D the flow tube internal diameter; (Španěl and Smith, 1996) ^c: calculated as $v_i = 1.5 \times v_g$; (Smith and Adams, 1988)
 282 ^d: estimated from the expression $t_r = \frac{L+\varepsilon}{v_i}$ where $\varepsilon = 1.5$ and corresponds to the distance for a full mixing of neutral
 283 molecules with the carrier gas in the flow tube; ^e: calculated using the recommended expressions by Hansel et al.
 284 (1997). $KE_{cm} = \frac{m+M}{M}(KE_{ion} - 1.5k_B T) + 1.5k_B T$ where m and M are the masses of the carrier gas and the neutral
 285 reactant, respectively, k_B is the Boltzmann constant and KE_{ion} is the kinetic energy of ions obtained by the expression
 286 $KE_{ion} = 1.5k_B T + 0.5mv_i^2 + 0.5M_{ion}v_i^2$, where M_{ion} is the mass of reactant ion; ^f: estimated using the following
 287 expression $[H_2O] = \frac{F_{H_2O}}{F_{total}} \times N$, where F_{H_2O} is the sample flow of pure water in the sample flow calculated as the
 288 product of RH with the total sample flow rate (35 mL min⁻¹), F_{total} the total flow rate inside the flow tube, and N the
 289 number density; ^g: calculated in a similar way with water concentrations, $[VOC] = \frac{F_{VOC}}{F_{total}} \times N$ where F_{VOC} is the sample
 290 flow of pure VOC in the sample flow calculated as the product of VOC mixing ratio in the total sample flow (35 mL
 291 min⁻¹).

292
 293 We observed that operating the instrument under SC or CC modes has a negligible impact on the
 294 concentration of the NO⁺ and O₂⁺ primary ions. However, the distribution of H₃O⁺ and H₃O⁺·H₂O clusters
 295 is influenced. The hydronium water cluster can be formed from (R1):



297 The rate coefficient of (R1) is $k_1(298 \pm 2K) = (6.55 \pm 0.75) \times 10^{-28}$ cm⁶ s⁻¹. It is an average value
 298 retrieved from three literature studies (Bierbaum et al., 1976; Bolden and Twiddy, 1972; Španěl and Smith,
 299 2001). The errors quoted correspond to the standard deviation of the measurements.

300
 301 Reaction 1 is an association reaction, and therefore the rate coefficient depends on the thermal stabilization
 302 of the adduct leading to the formation of H₃O⁺·H₂O, favored at low temperatures and high pressures.
 303 Consequently, both temperature and pressure modifications, applied to establish CC, enhance the formation
 304 of H₃O⁺·H₂O clusters. In addition, reaction time also plays a role. Under CC, t_r is increased by a factor of



305 1.22 compared to SC, and thus an increase in the concentration of $\text{H}_3\text{O}^+\cdot\text{H}_2\text{O}$ is expected. In order to
306 establish a criterion for the humidity adjustments during the calibration experiments and the different
307 operation modes of the instrument, the ratio of the signals for the $\text{H}_3\text{O}^+\cdot\text{H}_2\text{O}$ cluster at the m/z 37 (I_{37}) and
308 H_3O^+ at the m/z 19 (I_{19}) is considered. Note that similar approaches have been applied in literature. (Inomata
309 et al., 2008; Stönnner et al., 2017) In Fig. S1 are presented these relative ratios of I_{37}/I_{19} versus the RH in the
310 gas flow for the two different operation modes of the SIFT-MS. It should be noted that, as displayed in Fig.
311 S1 when ambient water vapor concentration is close to zero level, i.e. close to dry conditions, the I_{37}/I_{19}
312 ratio approaches zero pointing that the water coming from the discharge ion source entering the flow tube
313 is negligible compared to water vapor from the sampled dry air. This is in contrast with what has been noted
314 in PTR-MS studies (Inomata et al., 2008; Stönnner et al., 2017).

315

316 In theory, it is possible to estimate the water concentration inside the flow tube to better predict the changes
317 on the abundances of H_3O^+ and $\text{H}_3\text{O}^+\cdot\text{H}_2\text{O}$ ions. Lacko et al. (2020), applied the following expression to
318 estimate the water concentration:

319
$$[\text{H}_2\text{O}] = \frac{H}{t_r k_1} \quad \text{Eq. (2)}$$

320

321 where
$$H = \ln \frac{[\text{H}_3\text{O}^+] + [\text{H}_2\text{O}\cdot\text{H}_3\text{O}^+] + [(\text{H}_2\text{O})_2\cdot\text{H}_3\text{O}^+]}{[\text{H}_3\text{O}^+]} \quad \text{Eq. (3)}$$

322 However, in the literature, k_1 has solely been determined at room temperature, thus extrapolation cannot be
323 directly performed to SC or CC. Alternatively we can use the mixing ratios of water in the sample flow to
324 estimate the concentration of water molecules introduced in the flow tube (Table 1). The background $[\text{H}_2\text{O}]$
325 has been estimated in the range of 10^{10} molecule cm^{-3} , while the increase in RH resulted in water
326 concentrations introduced in the flow tube in the order of 10^{14} molecule cm^{-3} , corresponding to around 5 %
327 of the total number density. A similar approach was applied to estimate the concentrations of FM and GL
328 inside the flow tube. Using mixing ratios of 50 up to 1200 ppb in the sample flow, the concentrations of the
329 title VOCs were in the range of 10^8 molecule cm^{-3} , and thus several order of magnitude lower than $[\text{H}_2\text{O}]$.

330 **3.2 Formaldehyde Determination using SIFT-MS**

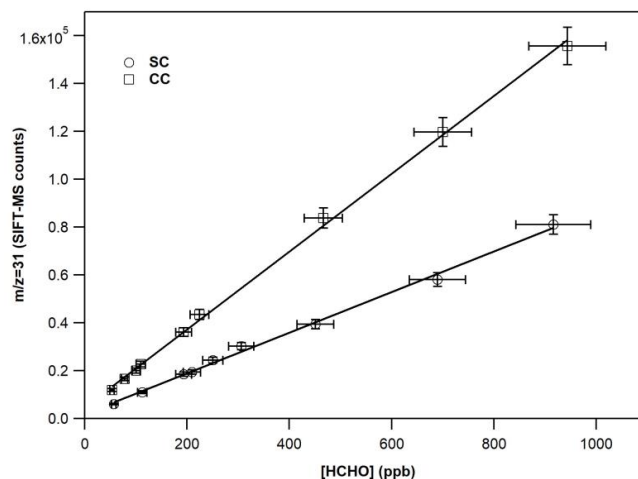
331

332 **3.2.1 Experimental Calibration of Formaldehyde under SC and CC**

333 Figure 3 displays typical calibration curves of FM operating SIFT-MS under standard and custom
334 conditions. The slope of the linear fit of experimental results corresponds to the calibration factor of the
335 compound of interest. In both cases, a linear response ($R^2 > 0.997$) of the instrument is noticed on the entire
336 concentration range explored. However, at 70% of RH the experimental data points are more scattered
337 resulting in a lower precision fit. In Table 2 are summarized the calibration factors at each I_{37}/I_{19} ratio.
338 Under CC, the sensitivity of SIFT-MS towards FM is increased by a factor of ca. 2, compared to SC. In
339 addition, considering the experimental uncertainties, under SC, the SIFT-MS response is not influenced by
340 the level of RH used while under CC the sensitivity of the instrument is reduced by a factor of 2 from dry
341 ($I_{37}/I_{19} < 0.01$) to 70% ($I_{37}/I_{19} = 1$). Actually, a careful look at the data presented in Table 2 points that SIFT-



342 MS sensitivity is not impacted by water presence when the relative ratio of I_{37}/I_{19} is below ca. 0.55,
 343 irrespectively of the SIFT-MS operation mode.
 344



345
 346

347 **Figure 3.** Calibration curves of FM at the m/z 31, derived from H_3O^+ precursor ion under dry conditions.
 348 The error bars on Y axis are 5 % (extreme value) and correspond to the 2σ standard deviation of the
 349 averaged value of the SIFT-MS signal for each measurement. The errors reported in X axis are 8 % and
 350 correspond to the uncertainty given for the cross section value of FM (4%) and other systematic
 351 uncertainties (in the flow of the mixture, sampling flow of the instrument, etc.) added in quadrature.

352 **Table 2.** Calibration factors and detection limits of FM at the $m/z = 31$ as a function of relative humidity
 353 for standard and custom operational conditions of the SIFT-MS. The calibration factor is derived from the
 354 slope of a typical experiments shown in Fig. 3. The errors given in the calibration factors are the 2σ precision
 355 of the linear fit.

RH gas flow (%)	Standard Operational Conditions			Custom Operational Conditions		
	I_{37}/I_{19}	Calibration factor (counts ppb ⁻¹)	Detection limits (ppt)	I_{37}/I_{19}	Calibration factor (counts ppb ⁻¹)	Detection limits (ppt)
Dry	0.001	84.8±3.8	400	0.005	163±4	100
10	0.09	88.4±6.2		0.28	148±6	120
30	0.26	83.0±2.2		0.56	145±4	
50	0.41	82.7±1.0		0.79	115±5	145
70	0.54	70.0±12	500	1.0	82.5±14	200



356 Contrariwise, in literature it is reported that the sensitivity of a PTR-MS is massively reduced with RH. For
357 instance, in the study of Stönnner et al. (2017), the PTR-MS sensitivity was reduced by a factor of five or
358 even greater when the relative ratio of $\text{H}_3\text{O}^+\cdot\text{H}_2\text{O}$ to H_3O^+ masses (measured as I_{39}/I_{21}) varies from <0.1 to
359 0.4.

360 3.2.2 Comparison of Formaldehyde Determination between SIFT-MS and PTR-MS

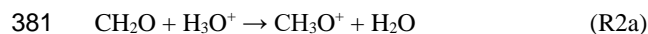
361 The contrasted behavior between the SIFT-MS and PTR-MS instruments are related to their distinct
362 operational principles and chemical reactions. Therefore, before getting into the chemistry of proton transfer
363 reactions for FM measurement, it is essential to discuss the major differences between the conditions inside
364 the flow tube of the SIFT-MS used in the current study and inside the drift tube of the PTR-MS instruments
365 deployed in literature for FM characterization (Inomata et al., 2008; Stönnner et al., 2017; Vlasenko et al.,
366 2010; Warneke et al., 2011).

367
368 The pressure inside the flow tube of the voice 200 Ultra SIFT-MS instrument ranges between 0.6 to 0.9
369 Torr (Table 1), which is by a factor of two lower than the pressure inside the drift tube in a PTR-MS. This
370 pressure difference can impact the ion chemistry and mainly the formation of $\text{H}_3\text{O}^+\cdot\text{H}_2\text{O}$ clusters. Besides
371 pressure, the main difference between the two instruments relies in the mean relative kinetic energy of
372 reactants (KE_{cm}). In the flow tube of the SIFT-MS the KE_{cm} of analytes and precursor ions depend mainly
373 on the temperature of the tube. Under the SC and CC the kinetic energy was calculated to be ca. 0.05 and
374 0.04 eV respectively (Table 1). On the contrary the application of an electrical field inside the drift tube of
375 a PTR-MS leads to significantly higher KE_{cm} values, reducing the sensitivity of the instrument. Typical
376 values of KE_{cm} range between 0.10 to 0.23 eV in studies using PTR-MS for formaldehyde monitoring (
377 Table 3), (Inomata et al., 2008).

378

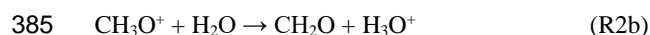
379 Ion Chemistry Involved in Formaldehyde Measurement with H_3O^+ Precursor Ion

380 The proton transfer reaction in case of FM can occur according to the following reaction:



382 The rate coefficient of (R2a), k_{2a} is in the order of $3 \times 10^{-9} \text{ cm}^3 \text{ s}^{-1}$ at $297 \pm 3 \text{ K}$ (Michel et al., 2005) (Table
383 3), and slightly dependent on KE_{cm} .

384 However, due to the low exothermicity of (R2a) the back reaction is also possible:



386 Hansel et al. (1997) evidenced that (R2b) is strongly dependent on the KE_{cm} values of reactants. The highest
387 the KE_{cm} of protonated formaldehyde (FM- H^+), the highest the probability for a successful collision. Thus,
388 the rate coefficient of deprotonization reaction k_{2b} increases. Table 3 summarizes the values of k_{2b} for
389 different KE_{cm} used in PTR-MS studies and under SC or CC conditions of the SIFT-MS. Furthermore,
390 (R2b) also depends on the concentration of water molecules when evaluating the response of the SIFT-MS
391 and PTR-MS instruments as a function of RH. Therefore, the contribution of these two parameters, i.e.
392 KE_{cm} of reactants and water concentration inside the reaction tubes, may explain the contrasted behaviors
393 between the two instruments. In SIFT-MS, due to the low kinetic energy of reactants, the protonation of
394 formaldehyde is strongly favored. Indeed, k_{2a}/k_{2b} ratio is ca.1600 and ca.5300 respectively under SC and



395 CC. It has to be noted that an increase of water concentration due to RH variation in the analytes shows a
 396 negligible impact on the k_{2a}/k_{2b} ratio. It can also be suggested that the higher k_{2a}/k_{2b} ratio under CC could
 397 explain the amplification by a factor of ca. 1.9 of FM sensitivity compared to SC. On the contrary, in the
 398 case of PTR-MS where higher kinetic energies are achieved, the relative ratio of k_{2a}/k_{2b} remains below 160
 399 and possibly goes down to 26. Thus, a substantial increase of water concentration makes (R2b) more
 400 impactful and the sensitivity of the instrument is strongly decreased.

401 **Table 3.** Rate coefficients of ion-molecule chemical reactions of formaldehyde under typical PTR-MS
 402 studies retrieved from literature and the conditions where SIFT-MS is deployed in this work.

Values	PTR-MS ^a			SIFT-MS	
				Standard operational conditions	Custom operational conditions
KE_{cm} (eV)	0.10	0.17	0.23	0.05	0.04
k_{2a} (10^{-9} cm ³ s ⁻¹)	1.6	1.4	1.3	3.2 ^b	3.2
k_{2b} (10^{-11} cm ³ s ⁻¹)	1.0	2.9	5.0	0.2 ^b	0.06 ^c
k_{3a} (10^{-9} cm ³ s ⁻¹)	-	-	-	2.65±0.35 ^d	-
k_{3b} (10^{-10} cm ³ s ⁻¹)	-	-	-	4.4±1.1	-
k_4 (10^{-11} cm ³ s ⁻¹)	negligible			1.2	>1.2
k_{2a}/k_{2b}	160	48	26	1600	5333
k_4/k_{2b}	negligible			6	>20

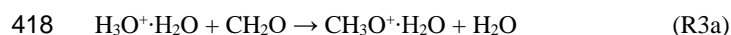
403 ^a: data retrieved from the work of Inomata et al. (2008). Authors extracted the k_{2a} and k_{2b} values based on the work of
 404 Hansel et al. (1997); ^b: average value determined by Hansel et al. (1997); ^c calculated by Bohme et al. (1979); ^d:
 405 average literature value from the studies of Bohme et al. (1979) and Midey et al. (2000). The error corresponds to the
 406 standard deviation of the measurements.

407 Although solely the $m/z = 31$ is used to monitor FM, in SIFT-MS other ion reactions can occur and form a
 408 protonated methyl hydroperoxide (PMH) complex with $m/z = 49$ (Hansel et al., 1997). These ion reactions
 409 are not expected to occur in PTR-MS due to the high KE_{cm} values. These reactions are strongly dependent
 410 on water concentrations in the flow tube, and they are competitive to (R2a) and (R2b). However, their
 411 contribution to the ion chemistry inside the flow tube of the SIFT-MS is expected to be of minor importance,
 412 especially under SC. Indeed, under SC the calibration factor of formaldehyde is not impacted by increasing
 413 water concentration by almost 540 times (considering the I_{37}/I_{19} ratios calculated under dry and 70 % of

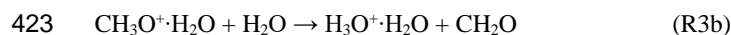


414 RH). However, since their occurrence cannot be excluded and they could play a role for I_{37}/I_{19} ratios above
415 0.55, these reactions are discussed in the following of the manuscript.

416 The protonation of formaldehyde can occur through ligand switching from the hydronium water cluster,
417 $\text{H}_3\text{O}^+\cdot\text{H}_2\text{O}$ and to form PMH through the following reaction:

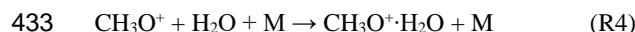


419 At room temperature, the rate coefficient of this reaction has been estimated to be $(2.65\pm 0.35)\times 10^{-9} \text{ cm}^3 \text{ s}^{-1}$
420 calculated from the average of literature values, (Bohme et al., 1979; Midey et al., 2000), and the error
421 corresponds to the standard deviation of the measurements. The rate coefficient of the back reaction (R3b)
422 was estimated to be around six times lower $(4.4\pm 1.1)\times 10^{-10} \text{ cm}^3 \text{ s}^{-1}$



424 Reaction 3 is expected to be highly sensitive on RH, i.e. the water concentrations in the flow tube. On one
425 side, the increase in water concentration will increase the concentration of $\text{H}_3\text{O}^+\cdot\text{H}_2\text{O}$ enhancing (R3a), on
426 the other side the excess of water compared to FM enhances (R3b). Therefore, the impact of (R3) in the ion
427 chemistry occurring in the flow tube of SIFT-MS is linked with the relative ratio of I_{37}/I_{19} . However, as
428 abovementioned, under SC the calibration factor at m/z 31 remains constant within the experimental
429 uncertainties, and thus (R3) seems to have insignificant impact on the sensitivity of the instrument.
430 However, in case of CC where the I_{37}/I_{19} is greater than 0.55, the gradual reduction in FM sensitivity could
431 be due to the competition between (R2a) and (R3a).

432 An alternative pathway of PMH formation is through (R4) in presence of a third body and water molecules:



434 Reaction 4 is an association reaction competitive with (R2b) and depends on the total pressure of the
435 reaction system and the kinetic energy of reactants. In the presence of a third body, the protonated
436 formaldehyde and water molecules can lose part of their energy through collisions and further stabilize to
437 form PMH increasing the rate coefficient k_4 . Therefore, it is expected that the rate coefficient of this
438 association reaction is enhanced with increasing pressure. Under a given pressure, k_4 is reduced as KE_{cm}
439 increases because the third body fails to stabilize reactants. Hansel et al. (1997) have studied the pressure
440 dependence of the rate coefficient k_4 at 0.05 eV; i.e. with KE_{cm} values similar with SIFT-MS SC used in the
441 present study. The rate coefficient of the ternary association at room temperature proposed by these authors
442 was $k_4 = 5.7 \times 10^{-28} \text{ cm}^6 \text{ s}^{-1}$. They concluded that for KE_{cm} greater than 0.06 eV k_4 is negligible compared
443 to k_{2b} . For that reason, this reaction is not taken into account in most of PTR-MS studies. Nevertheless, (R4)
444 could contribute to SIFT-MS response.

445 Indeed, we estimated that under SC and CC of SIFT-MS, the binary rate coefficient of the association
446 reaction at room temperature and the established pressures is greater than $1.2 \times 10^{-11} \text{ cm}^3 \text{ s}^{-1}$ and thus higher
447 than k_{2b} (Table 3). This value is calculated as the product of k_4 with the number density inside the flow tube
448 of SIFT-MS. However it remains around 260 times lower than formaldehyde protonation. At this point it
449 should be noted that the value of $1.2 \times 10^{-11} \text{ cm}^3 \text{ s}^{-1}$ should be considered as an upper limit of the contribution
450 of k_4 reaction, since under both SC and CC the flow tube was operated above room temperature, and thus
451 lower rate coefficient for k_4 is anticipated (ternary association reactions decrease with increasing



452 temperature). The importance of (R4) is expected to be enhanced at high water concentrations. Hansel et
453 al. (1997), reported that k_4 is increasing from dry to low concentrations of water reaching a maximum value,
454 and then decreases with the extra addition of water due to (R3b), which is around 37 times faster than (R4).
455 Note that absolute values cannot be extrapolated from their data. To determine the role of (R4) it is essential
456 to remind that it is competitive with (R1) for hydronium ion formation. Although k_1 has not been determined
457 for the temperatures of 323 and 393 K, considering that H_3O^+ is in high excess compared to FM, (R1) is
458 expected to be the dominant.

459 **Wrap up on Formaldehyde Determination**

460 In the case of SIFT-MS, the ion chemistry of formaldehyde is mainly controlled by (R2a) and (R2b). The
461 increased sensitivity observed under CC conditions is mainly linked to the higher k_{2a}/k_{2b} values achieved
462 compared with SC. The low kinetic energy of reactants in SIFT-MS flow tube is the reason why the
463 sensitivity of the instrument is not significantly impacted by RH. This behavior contrasts with PTR-MS.
464 (R3) and (R4), involving PMH production and inducing a lower sensitivity at the mass peak 31, seem to be
465 of minor importance or at least to be in equilibrium state for I_{37}/I_{19} below 0.55. Above that threshold, their
466 occurrence could explain a lower sensitivity but this point needs further investigations to be experimentally
467 validated. The detection limit of formaldehyde is 450 ± 50 ppt under SC. The CC allow decreasing the
468 detection limits of the SIFT MS instrument by a factor of ca. 4 for 0-50% RH (100 ppt) and by a factor of
469 2 under 70 % RH (200 ppt) (Table 2). These detection limits, based on a signal to noise ratio $S/N = 3.3$, are
470 comparable or lower than those reported in the PTR-MS studies that mentioned DL between 200-500 ppt
471 with $S/N = 2$, (Inomata et al., 2008), and DL 100 ppt under dry and 300 ppt under humid using $S/N = 1$,
472 (Warneke et al., 2011), and close to the most performant spectroscopic techniques noting DL around 80 ppt
473 (Catoire et al., 2012; Winkowski and Stacewicz, 2020).

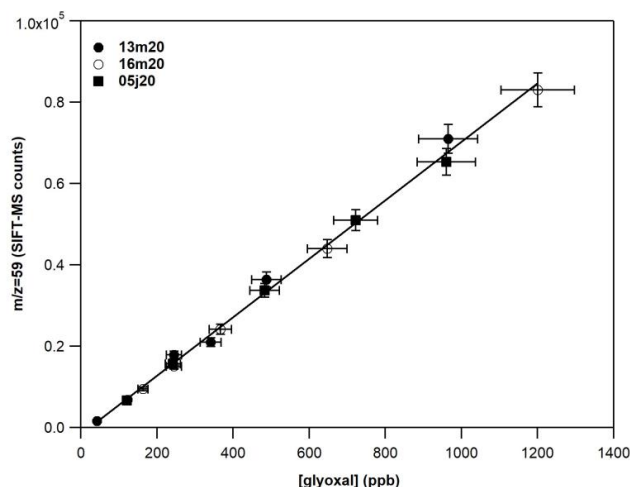
474 **3.3 Glyoxal Determination with SIFT-MS.**

475

476 This section is dedicated to the evaluation of the performances of the SIFT-MS instrument to determine GL
477 in the ppb range as a function of RH. To that end, SIFT-MS is operated under both SC and CC, with a focus
478 on the chemistry of H_3O^+ and NO^+ ions. Note that, O_2^+ ion is not considered in the present study, due to
479 significant fragmentation of molecular GL induced by this ions and a subsequent lower sensitivity, strongly
480 impacted by RH.

481 **3.3.1. Experimental Calibration of Glyoxal as a Function of RH**

482 Figure 4 displays a typical calibration experiment of GL deploying SIFT-MS under SC and recording the
483 mass peak 59 ($\text{C}_2\text{H}_3\text{O}_2^+$) with H_3O^+ as precursor ion. A linear response ($R^2 > 0.999$) of the instrument is
484 noticed on the entire concentration range explored. The data points presented in Fig. 4 are obtained from
485 two different GL syntheses and on three different days dispatched on three months. Table 4 summarizes
486 the calibration factors and corresponding uncertainties retrieved for the mass peaks used to record GL under
487 SC and CC.



488

489 **Figure 4.** Calibration curves of GL at the m/z 59 derived from H_3O^+ precursor ion under dry conditions.
 490 The error bars on Y axis are 5% (extreme value) and correspond to the 2σ standard deviation of the averaged
 491 value of the SIFT-MS signal for each measurement. The errors in X axis are 8% and corresponds to the
 492 uncertainty given for the cross section value of GL (4%) and other systematic uncertainties (in the flow of
 493 the mixture, sampling flow of the instrument, etc.) added in quadrature. Circles corresponds to experiments
 494 carried out on different days (13 March 2020 and 16 March 2020) from the same gas mixture. Squares
 495 correspond to experiments carried out almost three months later (5 June 2020) with a new gas mixture and
 496 synthesis of GL.

497 **Table 4.** Calibration factors and relative ratios determined for GL under SC and CC at the m/z 59 ($C_2H_3O_2^+$)
 498 and m/z 88 ($C_2H_2O_2 \cdot NO^+$) using the H_3O^+ and NO^+ precursor ions respectively. The errors quoted
 499 correspond to the 2σ precision of the fit to obtain the calibration factors.

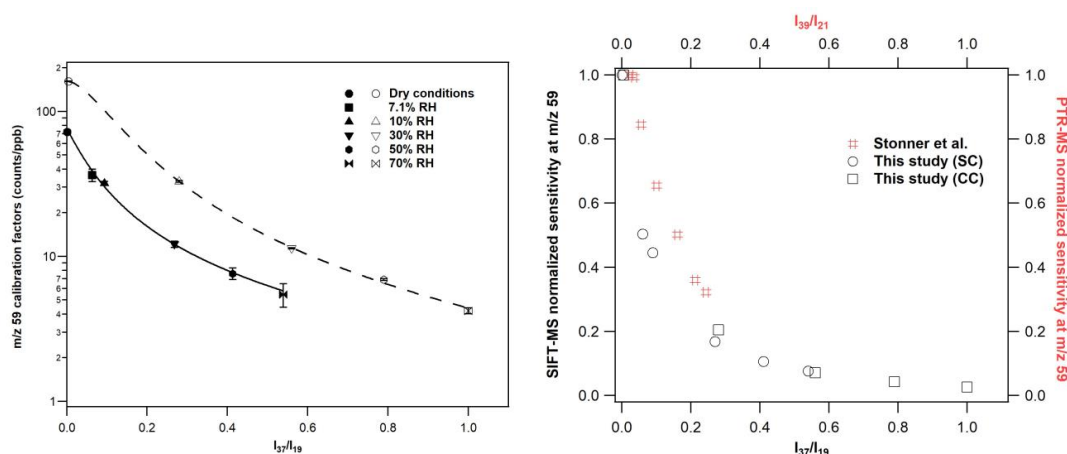
Standard Conditions (SC)				Custom Conditions (CC)			
I_{37}/I_{19}	Calibration factors (counts ppb ⁻¹)		Relative ratios	I_{37}/I_{19}	Calibration factors (counts ppb ⁻¹)		Relative ratios
	m/z 59 (H_3O^+)	m/z 88 (NO^+)	I_{59}/I_{88}		m/z 59 (H_3O^+)	m/z 88 (NO^+)	I_{59}/I_{88}
0.001	71.9±2.4	0.41±0.02	175	0.005	161±1	3.20±0.06	50.3
0.06	36.2±3.6	0.45±0.03	81.0	-	n.d ^b	n.d	n.d
0.09	32.0±0.9	0.44±0.03	72.7	0.28	32.9±0.5	3.41±0.07	9.6
0.27	12.1±0.6	0.48±0.05	25.2	0.56	11.4±0.1	3.68±0.18	3.1
0.41	7.6±0.7	0.50±0.03	15.2	0.79	6.9±0.1	4.30±0.05	1.6



0.54	5.5±1.0	0.52±0.02	10.5	1	4.2±0.2	4.47±0.07	0.94
------	---------	-----------	------	---	---------	-----------	------

500 Considering the H_3O^+ precursor ion and the mass peak 59, an increase of the sensitivity of the instrument
 501 by a factor of 2 is noticed under CC compared to SC (left panel of Fig. 5). Note that a similar enhancement
 502 is observed for FM (Figure 3 and Table 2). Nevertheless, the sensitivity is diminished with increasing RH
 503 under both SC and CC. To evaluate whether the impact of water to GL detection is similar under both
 504 operational conditions, we plotted the normalized sensitivity (calibration factor dry / calibration factor
 505 humid) versus I_{37}/I_{19} ratios. , and results are also displayed in Fig. 5 (right panel). It seems that the impact
 506 of water to the sensitivity of the instrument at the mass peak 59 is similar for both SC and CC. Under dry,
 507 the detection limits for GL at the mass peak 59 are determined as 280 ± 30 ppt and 120 ± 12 ppt for SC and
 508 CC respectively for 1 minute integration time (Table S1 and S2). Nevertheless, with the increase of relative
 509 humidity to 70% detection limits are increased up to 6 ± 1 ppb.

510



511
 512
 513

514 **Figure 5.** Left panel: calibration factors of GL at m/z 59 derived from H_3O^+ precursor ion under SC (filled
 515 symbols) and CC (open symbols) conditions. The errors quoted correspond to the 2σ precision of the fit to
 516 obtain the calibration factors. The lines are the fitting of calibration factors with the empirical expression:
 517 $calibration\ factor = \frac{a}{b + (\frac{I_{37}}{I_{19}})^c}$ where for SC $a=2.99$, $b=0.04$, $c=1.20$ and CC $a=4.53$, $b=0.03$, $c=1.74$.

518 Right panel: GL normalized sensitivity at the mass peak 59 of SIFT-MS (in black) and PTR-MS (in red)
 519 versus the I_{37}/I_{19} and I_{39}/I_{21} ratios. For SIFT-MS, the reduction to instrument sensitivity is similar for both
 520 SC and CC conditions. For comparison purposes, the data presented in Fig. 5 of Stöner et al. (2017) study
 521 were extracted and displayed in the graph. A steeper decrease to GL sensitivity is noticed with SIFT-MS at
 522 low levels of humidity than PTR-MS.

523

524 The detection of GL was also achieved using the NO^+ precursor ion at the mass peak 88. Table 4 displays
 525 the calibration factors determined. Under SC we noticed a weaker response of the instrument using the NO^+
 526 precursor ion compared to H_3O^+ ion. Remarkably, the introduction of water had no significant impact on
 527 the sensitivity of the mass peak 88. In fact, at the highest RH corresponding to $I_{37}/I_{19} = 0.54$, the instrument



528 was 20% more sensitive than under dry. Operating the instrument under CC, increased by a factor of eight
529 the sensitivity at the mass peak 88. Again, the introduction of water improved the detection of GL at the
530 mass peak 88, by around 28% this time. Interestingly, as displayed in Table 4 at high water concentrations,
531 peak 88 is more sensitive than mass peak 59.

532

533 3.3.2. Comparison of Glyoxal Determination between SIFT-MS and PTR-MS

534 There are only a few studies in literature exploring the measurement of Glyoxal using PTR-MS. Thalman
535 et al. (2015) performed a thorough inter-comparison study of spectrometric and spectroscopic techniques
536 for the detection of GL in an atmospheric simulation chamber. In their experiments authors used
537 concentrations of GL up to 32 ppb, but they were unable to detect GL with their PTR-MS, attesting of the
538 low sensitivity of the instrument (Thalman et al., 2015). However, in the recent study of Stönner et al.
539 (2017), GL was detected at low concentrations deploying an Ionicon PTR-TOF-MS-8000 instrument.
540 Interestingly these authors observed a decreasing sensitivity of the PTR-MS instrument with increasing
541 water concentration, similarly to our study. As can be seen in Fig. 5 the decrease in GL sensitivity at the
542 mass peak 59 is steeper in our SIFT-MS compared with PTR-MS (data are also presented in Table S3).
543 Stönner et al. (2017), estimated the detection limits for GL at 250 ppt under dry and 700 ppt at the highest
544 level of RH used.

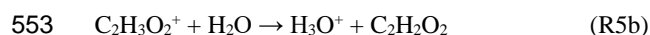
545

546 Ion Chemistry Involved in Glyoxal Measurement with H_3O^+ Precursor Ion

547 Considering the ion chemistry of H_3O^+ , the protonation of glyoxal can occur through the following
548 reaction:



550 The rate coefficient of (R5a), k_{5a} is $1.9 \times 10^{-9} \text{ cm}^3 \text{ s}^{-1}$ and is competitive with hydronium formation (reaction
551 1). Due to the low proton affinity of GL the deprotonization reaction is expected to occur as reported by
552 (R5b):

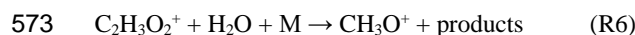


554 The rate coefficient of (R5b) has not been determined in literature, it could depend on KE_{cm} , similarly to
555 (R2b). Considering this scenario, the increased sensitivity of the instrument under CC could be due to higher
556 k_{5a}/k_{5b} relative ratios, similarly to what is noticed for FM. The decreasing sensitivity of the SIFT-MS with
557 increasing water concentration could be also due to the competition between (R5a) and (R5b). In this case,
558 (R5b) should be relatively fast even under dry conditions. Its impact would be enhanced with the addition
559 of water to the reaction system, leading to initial reactants. Note that Stönner et al. (2017) made a similar
560 hypothesis to explain the decreased sensitivity with water concentration of their PTR-MS.

561 Another plausible explanation for the decreasing sensitivity of the SIFT-MS with increasing RH could be
562 the fragmentation of protonated GL ($\text{C}_2\text{H}_3\text{O}_2^+$ or GL-H^+) to protonated FM (CH_3O^+ or FM-H^+) inside the
563 flow tube. The latter has been observed in the drift tube of the PTR-MS used by Stönner et al (2017).
564 Authors report a considerably larger signal on FM-H^+ than GL-H^+ . In a recent study, Lacko et al. (2020)
565 studied the fragmentation of protonated GL deploying a SIFT-MS. The authors evidenced the strong impact
566 of water concentration on GL-H^+ fragmentation leading to FM-H^+ . Interestingly, they have not observed
567 FM-H^+ under dry conditions. Thus, authors proposed that it should be formed only in the presence of water.
568 Similar conclusions are reported by Michel et al. (2005). Finally, Lacko et al. (2020) combined their

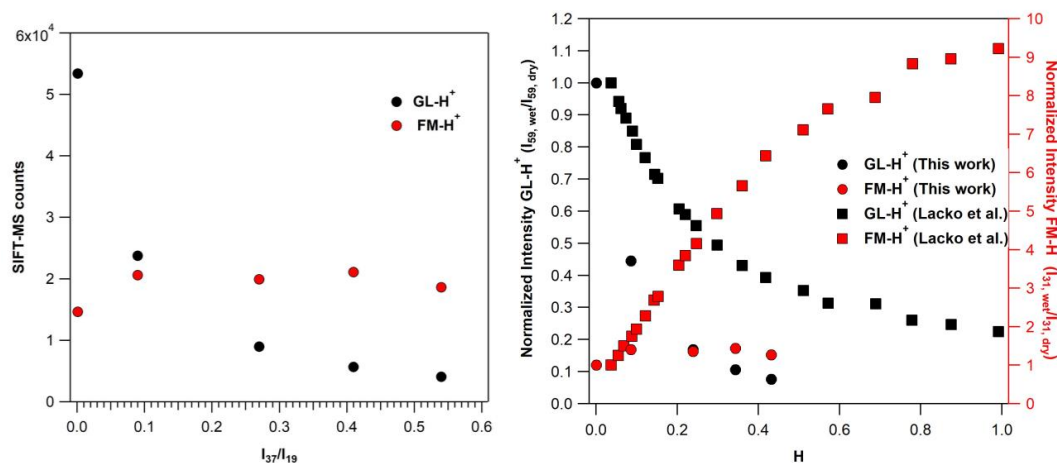


569 experimental observations with numerical modeling and proposed a sequence of reactions to explain the
570 fragmentation of GL-H^+ to FM-H^+ . The discussion of these reaction pathways is beyond the scope of this
571 study, nevertheless to feed the discussion of the manuscript we present them with the following simple
572 expression reported by (R6):



574 In this study we have also investigated the possible fragmentation of GL-H^+ to FM-H^+ . These experiments
575 have been performed under both SC and CC. Note that our observations were found to be independent of
576 GL concentration introduced. First we discuss our observations under SC and then under CC. The left panel
577 of Fig. 6 displays the variation of the signals recorded for FM-H^+ and GL-H^+ with I_{37}/I_{19} ratios. For
578 comparison purposes we present the normalized signals versus H factor as determined in the study of Lacko
579 et al. (2020), i.e. Eq. (3), in the right panel of Fig. 6 (data are also given in Table S4).

580 **Fragmentation of GL-H^+ under SC and dry.** In contrast with the work of Lacko et al, we observe the
581 formation of FM-H^+ even under dry conditions, (Lacko et al., 2020).



582

583 **Figure 6.** Left panel: SIFT-MS counts at the mass peak 59 (in black) of GL-H^+ and mass peak 31 (in red)
584 of FM-H^+ recorded by the SIFT-MS under SC conditions using around 750 ppb of GL operating the
585 instrument under SC. Right panel: Normalized sensitivity at the mass peak 59 (in black) of GL-H^+ and
586 mass peak 31 (in red) of FM-H^+ , recorded with SIFT-MS under SC based on the results of the current study
587 (circles) and Lacko et al. (2020) (squares, data extracted from their Fig. 3) versus the H value Eq. (3).

588 The FM-H^+ signal recorded corresponds to 27 % of GL-H^+ . Therefore, it is possible that in our SIFT-MS,
589 FM-H^+ is formed through alternative pathways. We propose that under our experimental conditions, GL-H^+
590 can either thermally decompose inside the flow tube (operated at 393 K under SC, Table 1) or
591 fragmentizes through collisions with ions inside the flow tube leading to FM-H^+ (R7). Both pathways are
592 expected to be enhanced at higher temperatures and higher KE_{cm} . Note that GL-H^+ thermal fragmentation
593 is expected to be significantly lower in the system of Lacko et al. (2020) where the flow tube temperature
594 was 300 K, as well as in the PTR-MS where the drift tube temperature was set to 333 K and higher pressure
595 (Stönnner et al., 2017).



597 We expect that both the thermal decomposition and collision fragmentation pathways are independent of
598 the water concentration inside the SIFT flow tube. At this point it should be noted that possible thermal
599 decomposition of molecular GL in the sample plate or inside the flow tube should be considered negligible.
600 In particular, the most probable thermal decomposition pathway of molecular GL is through the following
601 reaction (Saito et al., 1984):



603 The molecular FM could then react with H_3O^+ through (R2a) and lead to the formation of $FM-H^+$. However,
604 the energy barrier for the thermal decomposition of the lowest transition state to give products in (R8) is
605 around 230 kJ mol^{-1} (Koch et al., 2001). Therefore, it is unlikely to occur at these temperatures and in our
606 system. To further validate this point, we have performed a series of experiments introducing GL inside the
607 optical cell of the FTIR spectrometer operated at 393 K and recording sequential spectra of GL for several
608 hours. No thermal decomposition was noticed as previously reported in literature (Feierabend et al., 2008).
609

610 **Fragmentation of $GL-H^+$ under SC and humid.** Increasing the water concentration from dry to 10 % of
611 RH (corresponding to an increase by a factor of 90 to the I_{37}/I_{19} ratios, Table 4) the signal of $GL-H^+$ is
612 reduced by 56 %, while the formation of $FM-H^+$ is enhanced by 40% (see also Fig. 6). This clearly shows
613 that water plays a role in the formation of $FM-H^+$ to the reduced sensitivity of GL and processes proposed
614 by Lacko et al. (2020), (R6) are probably taking place. Further increase of water concentrations in the flow
615 tube had no impact on the formation $FM-H^+$ but GL sensitivity is still reduced. Essentially, using SIFT-MS
616 under SC conditions, the formation of $FM-H^+$ is less impacted by water concentrations than other literature
617 studies. Indeed, as displayed in the right panel of Fig. 6 although the GL sensitivity loss is steeper in our
618 study compared to Lacko et al. (2020), the corresponding formation of $FM-H^+$ is substantially lower
619 To conclude under SC conditions, the fragmentation of $GL-H^+$ to $FM-H^+$ occurs in the flow tube of the
620 SIFT-MS, but it is less impacted by water concentrations than PTR-MS. Alternatively, we propose that $GL-H^+$
621 decomposes either thermally or through ion collisions leading to $FM-H^+$. Therefore, it seems that the
622 abrupt loss of GL sensitivity with water concentrations is mainly due to the competition of (R5a) and (R5b).
623 Especially under the temperature of 393 K, the deprotonization (R5b) is expected to be faster than room
624 temperature and to play a more significant role than in the work of Lacko et al. (2020).
625

626 **Fragmentation of $GL-H^+$ under CC and dry.** Under custom conditions (CC) of the SIFT-MS, the formation
627 of protonated formaldehyde from the fragmentation of $GL-H^+$, is also observed. Nevertheless, the ratio of
628 $FM-H^+$ to $GL-H^+$ signals is significantly diminished. Indeed, under dry conditions the fragmentation is
629 reduced from 27 % to 12 % for SC and CC respectively. This observation supports our previous hypothesis:
630 $GL-H^+$ could decompose inside our SIFT-MS flow tube. Both the temperature decrease and pressure
631 increase, changing from SC to CC, tend to suppress the decomposition of protonated GL.
632

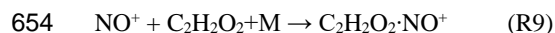
633 **Fragmentation of $GL-H^+$ under CC and humid.** A similar reduction of the fragmentation of $GL-H^+$ was
634 noticed in presence of water when comparing the signals recorded under SC and CC for I_{37}/I_{19} equal to
635 0.27 ± 0.01 and 0.55 ± 0.01 . As displayed in Fig. S2 the decreased sensitivity of GL is similar under both SC
636 and CC. Note that Fig. S2 should be viewed as a way to compare the impact of water concentrations on the
637 fragmentation of $GL-H^+$ and the appearance of $FM-H^+$. Essentially, the impact of water to the sensitivity of



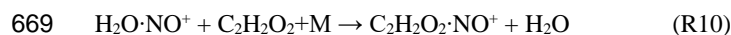
638 SIFT-MS to GL is independent on the operational conditions of the instrument. However, with the increase
639 of water concentration inside the flow tube from dry to a value of 0.28 for I_{37}/I_{19} ratio (an increase by a
640 factor of 56) the signal of protonated formaldehyde increases by almost a factor of 3. Therefore, water plays
641 a more important role to the presence of FM-H⁺ under CC and we anticipate that reactions proposed by
642 Lacko et al. (2020) can dominate (R6). Further increase of water concentration in the flow tube reduced the
643 signal of FM-H⁺. Although this looks as a paradox and in contradiction with the abovementioned
644 discussion, we suggest that this decrease is related to the competition between the (R6) and (R7), i.e. the
645 deprotonization reaction of FM-H⁺ (R2b). Nevertheless, a more thorough investigation is necessary to
646 support this point.
647 Therefore, we propose that the increased sensitivity of the instrument under CC is mainly due to higher
648 k_{5a}/k_{5b} ratios. The expected lower values of this k_{5a}/k_{5b} ratio could explain the lower sensitivity to detect GL
649 in the presence of water. Nevertheless, the decreasing GL sensitivity with increasing RH could be also
650 attributed to fragmentation of GL-H⁺ to FM-H⁺, both linked to thermal decomposition and reactions
651 involving water molecules as discussed by Lacko et al. (2020).

652 **Ion Chemistry Involved in Glyoxal Measurement using NO⁺ Precursor Ion**

653 The detection of GL in the flow tube of the SIFT-MS proceeds through the following reaction:



655 The rate coefficient measured at room temperature for (R9) is $8 \times 10^{-11} \text{ cm}^3 \text{ s}^{-1}$, (Michel et al., 2005) i.e.
656 around 24 times below the protonation reaction of GL (R5a). The latter could explain the reduced sensitivity
657 at the mass peak 88 compared to the mass 59 under dry conditions. Furthermore, (R9) is a three-body
658 association reaction. In an association process, an intermediate species is formed before the formation of
659 final products. The stability of this intermediate is both temperature and pressure dependent, and determines
660 the overall rate coefficient of the reaction. The increased sensitivity to the detection of GL under custom
661 conditions, is related with the temperature and pressure conditions existing in the flow tube. In particular
662 the flow tube temperature decrease combined with a 20% increase in the total pressure (from 0.65 to 0.85
663 Torr) resulted in a better stabilization of the adduct that leads to product formation for (R9), and thus
664 improved sensitivity. Apparently under our experimental conditions the reaction of NO⁺ with GL is in the
665 exponential part of a typical fall-off graph of an association reaction (Guimbaud et al., 2007).
666 The positive impact of water concentrations on the detection of GL at the mass peak 88, could be linked
667 with the formation of H₂O·NO⁺ hydrate cluster at the mass peak 48. Indeed, we have observed an increase
668 to the abundance of the cluster with increasing RH. The following reaction could be proposed:



670 Although the rate coefficient of (R9) has not been measured in literature, it has been showed that the
671 reactions of H₂O·NO⁺ with several VOCs are just as fast as or even faster than those with NO⁺ ion (Michel
672 et al., 2005).



673 4. Conclusions

674 SIFT-MS appears to be a powerful and reliable analytical tool for the real-time quantification of FM in
675 laboratory studies and outdoor/indoor field environments. This conclusion is based on the low detection
676 limits achieved, in the order of 100 to 500 ppt, and the remarkable stability of the instrument as a function
677 of relative humidity. Furthermore, our strategy to operate the SIFT-MS instrument under different modes,
678 allowed us to shed light on the ion chemistry occurring in the flow tube and to identify the key reactions
679 and processes that define the sensitivity of the instrument towards FM. A thorough comparison of our
680 observations with literature studies carried out with PTR-MS, evidences that the strong decay of PTR-MS
681 sensitivity with increasing RH is related to the application of the electrical field in the DRIFT tube. It
682 enhances the rate coefficient of deprotonation reaction of FM. Regarding GL, we have performed a
683 detailed research on the ion chemistry related with H_3O^+ and NO^+ ions. Regarding H_3O^+ we evidenced a
684 sharp decrease of the instrument sensitivity with increasing RH, similar to previous PTR-MS and SIFT-MS
685 studies, due to GL-H^+ fragmentation. Nevertheless, based on our experimental observations we propose
686 alternative pathways of GL-H^+ fragmentation, such as GL-H^+ decomposition, which seems to be of greater
687 importance than it has been considered previously in literature. Based on the detection limits achieved with
688 the H_3O^+ ion, we suggest that SIFT-MS is not able to monitor GL in outdoor ambient air due to the strong
689 impact of RH on GL sensitivity, but it can be deployed efficiently in indoor environments and laboratory
690 scale studies. In addition, we recommend that using the H_3O^+ ion for the monitoring of GL concentrations
691 should be performed with great caution due to the strong RH dependence and contribution on the signal of
692 FM-H^+ . Nevertheless, deploying NO^+ precursor ion for the monitoring of GL seems to be ideal since the
693 sensitivity of the instrument is slightly impacted by RH. The GL detection limits using NO^+ are in the ppb
694 range, however, we evidence that slight pressure increase in the flow tube of the instrument can result to a
695 vigorous increase to instrument sensitivity. Certainly, our research on the NO^+ chemistry opens new
696 pathways for GL quantification and detection in ambient air deploying soft ionization techniques, such as
697 PTR-MS with NO^+ ion, which are generally operated at higher pressures than SIFT-MS. Ultimately, our
698 observations indicate that there is potential for sensitivity improvement for the SIFT-MS, and that it should
699 be considered as a promising tool for the real-time monitoring of VOCs with low proton transfer affinity.

700 Data availability

701 All relevant data and supporting information have been provided in the Supplement.

702

703 Author contribution

704 AZ realization of experiments, data treatment. MNR designing of experiments, data treatment and
705 manuscript writing. FT designing of experiments and manuscript writing.

706

707 Competing interests

708 The authors declare that they have no conflict of interest.

709

710 Acknowledgements

711 This work was achieved in the frame of CLIMDO project funded by ANR under contract (ANR-19-CE01-
712 0008), Labex CaPPA, funded by ANR through the PIA under contract ANR-11-LABX-0005-01, and CPER



713 CLIMIBIO project, both funded by the Hauts-de-France Regional Council and the European Regional
714 Development Fund (ERDF).
715



716 References

717

- 718 Allani, A., Bedjanian, Y., Papanastasiou, D. K., and Romanias, M. N.: Reaction Rate Coefficient
719 of OH Radicals with d9-Butanol as a Function of Temperature, *ACS Omega*, 6, 18123-18134,
720 <https://doi.org/10.1021/acsomega.1c01942>, 2021.
- 721 Atkinson, R.: Atmospheric Chemistry of VOCs and NO_x, *Atmos. Environ.*, 34, 2063-2101,
722 [https://doi.org/10.1016/S1352-2310\(99\)00460-4](https://doi.org/10.1016/S1352-2310(99)00460-4), 2000.
- 723 Ban-Weiss, G. A., McLaughlin, J. P., Harley, R. A., Kean, A. J., Grosjean, E., and Grosjean, D.:
724 Carbonyl and Nitrogen Dioxide Emissions From Gasoline- and Diesel-Powered Motor Vehicles,
725 *Environ. Sci. Technol.*, 42, 3944-3950, <https://doi.org/10.1021/es8002487>, 2008.
- 726 Bernstein, R. S., Stayner, L. T., Elliott, L. J., Kimbrough, R., Falk, H., and Blade, L. E. O.:
727 Inhalation Exposure to Formaldehyde: An Overview of Its Toxicology, Epidemiology, Monitoring,
728 and Control, *Am. Ind. Hyg.*, 45, 778-785, <https://doi.org/10.1080/15298668491400601>, 1984.
- 729 Bierbaum, V. M., Golde, M. F., and Kaufman, F.: Flowing Afterglow Studies of Hydronium Ion
730 Clustering Including Diffusion Effects, *J. Chem. Phys.*, 65, 2715-2724,
731 <https://doi.org/10.1063/1.433415>, 1976.
- 732 Bohme, D. K., Mackay, G. I., and Tanner, S. D.: An Experimental Study of the Gas-Phase
733 Kinetics of Reactions with Hydrated Hydronium(1+) Ions (n = 1-3) at 298 K, *J. Am. Chem. Soc.*,
734 101, 3724-3730, <https://doi.org/10.1021/ja00508a003>, 1979.
- 735 Bolden, R. C. and Twiddy, N. D.: A Flowing Afterglow Study of Water Vapour, *Faraday Discuss.*
736 *Chem. Soc.*, 53, 192-200, <https://doi.org/10.1039/DC9725300192>, 1972.
- 737 Caron, A., Redon, N., Thevenet, F., Hanoune, B., and Coddeville, P.: Performances and
738 limitations of electronic gas sensors to investigate an indoor air quality event, *Build. Environ.*,
739 107, 19-28, <https://doi.org/10.1016/j.buildenv.2016.07.006>, 2016.
- 740 Caron, F., Guichard, R., Robert, L., Verrielle, M., and Thevenet, F.: Behaviour of individual
741 VOCs in indoor environments: How ventilation affects emission from materials, *Atmos. Environ.*,
742 243, 117713, <https://doi.org/10.1016/j.atmosenv.2020.117713>, 2020.
- 743 Catoire, V., Bernard, F., Mébarki, Y., Mellouki, A., Eyglunent, G., Daële, V., and Robert, C.: A
744 Tunable Diode Laser Absorption Spectrometer for Formaldehyde Atmospheric Measurements
745 Validated by Simulation Chamber Instrumentation, *J. Environ. Sci.*, 24, 22-33,
746 [https://doi.org/10.1016/S1001-0742\(11\)60726-2](https://doi.org/10.1016/S1001-0742(11)60726-2), 2012.
- 747 Coburn, S., Ortega, I., Thalman, R., Blomquist, B., Fairall, C. W., and Volkamer, R.:
748 Measurements of Diurnal Variations and Eddy Covariance (EC) Fluxes of Glyoxal in the
749 Tropical Marine Boundary Layer: Description of the Fast LED-CE-DOAS Instrument, *Atmos.*
750 *Meas. Tech.*, 7, 3579-3595, <https://doi.org/10.5194/amt-7-3579-2014>, 2014.
- 751 Crump, D. R., Squire, R. W., and Yu, C. W. F.: Sources and Concentrations of Formaldehyde
752 and Other Volatile Organic Compounds in the Indoor Air of Four Newly Built Unoccupied Test
753 Houses, *Indoor Built Environ.*, 6, 45-55, <https://doi.org/10.1177/1420326x9700600106>, 1997.
- 754 Feierabend, K. J., Zhu, L., Talukdar, R. K., and Burkholder, J. B.: Rate Coefficients for the OH +
755 HC(O)C(O)H (Glyoxal) Reaction between 210 and 390 K, *J. Phys. Chem. A.*, 112, 73-82,
756 <https://doi.org/10.1021/jp0768571>, 2008.
- 757 Fu, T.-M., Jacob, D. J., Wittrock, F., Burrows, J. P., Vrekoussis, M., and Henze, D. K.: Global
758 Budgets of Atmospheric Glyoxal and Methylglyoxal, and Implications for Formation of
759 Secondary Organic Aerosols, *J. Geophys. Res. Atmos.*, 113,
760 <https://doi.org/10.1029/2007JD009505>, 2008.
- 761 Gómez Alvarez, E., Moreno, M. V., Gligorovski, S., Wortham, H., and Cases, M. V.:
762 Characterisation and Calibration of Active Sampling Solid Phase Microextraction Applied to
763 Sensitive Determination of Gaseous Carbonyls, *Talanta*, 88, 252-258,
764 <https://doi.org/10.1016/j.talanta.2011.10.039>, 2012.



- 765 Grosjean, D., Grosjean, E., and Gertler, A. W.: On-Road Emissions of Carbonyls from Light-
766 Duty and Heavy-Duty Vehicles, *Environ. Sci. Technol*, 35, 45-53,
767 <https://doi.org/10.1021/es001326a>, 2001.
- 768 Guimbaud, C., Catoire, V., Bergeat, A., Michel, E., Schoon, N., Amelynck, C., Labonnette, D.,
769 and Poulet, G.: Kinetics of the reactions of acetone and glyoxal with O₂⁺ and NO⁺ ions and
770 application to the detection of oxygenated volatile organic compounds in the atmosphere by
771 chemical ionization mass spectrometry, *I. J. of Mass Spectrom.*, 263, 276-288,
772 <https://doi.org/10.1016/j.ijms.2007.03.006>, 2007.
- 773 Hansel, A., Singer, W., Wisthaler, A., Schwarzmann, M., and Lindinger, W.: Energy
774 Dependencies of the Proton Transfer Reactions H₃O⁺ + CH₂O ⇌ CH₂OH⁺ + H₂O, *Int. J. Mass
775 Spectrom. Ion Process*, 167-168, 697-703, [https://doi.org/10.1016/S0168-1176\(97\)00128-6](https://doi.org/10.1016/S0168-1176(97)00128-6),
776 1997.
- 777 Hays, M. D., Geron, C. D., Linna, K. J., Smith, N. D., and Schauer, J. J.: Speciation of Gas-
778 Phase and Fine Particle Emissions from Burning of Foliar Fuels, *Environ. Sci. Technol.*, 36,
779 2281-2295, <https://doi.org/10.1021/es0111683>, 2002.
- 780 Inomata, S., Tanimoto, H., Kameyama, S., Tsunogai, U., Irie, H., Kanaya, Y., and Wang, Z.:
781 Technical Note: Determination of Formaldehyde Mixing Ratios in air with PTR-MS: Laboratory
782 Experiments and Field Measurements, *Atmos. Chem. Phys.*, 8, 273-284,
783 <https://doi.org/10.5194/acp-8-273-2008>, 2008.
- 784 Kaiser, J., Wolfe, G. M., Bohn, B., Broch, S., Fuchs, H., Ganzeveld, L. N., Gomm, S., Häsel, R.,
785 Hofzumahaus, A., Holland, F., Jäger, J., Li, X., Lohse, I., Lu, K., Prévôt, A. S. H., Rohrer, F.,
786 Wegener, R., Wolf, R., Mentel, T. F., Kiendler-Scharr, A., Wahner, A., and Keutsch, F. N.:
787 Evidence for an Unidentified Non-Photochemical Ground-Level Source of Formaldehyde in the
788 Po Valley with Potential Implications for Ozone Production, *Atmos. Chem. Phys.*, 15, 1289-
789 1298, <https://doi.org/10.5194/acp-15-1289-2015>, 2015.
- 790 Kean, A. J., Grosjean, E., Grosjean, D., and Harley, R. A.: On-Road Measurement of Carbonyls
791 in California Light-Duty Vehicle Emissions, *Environ. Sci. Technol*, 35, 4198-4204,
792 <https://doi.org/10.1021/es010814v>, 2001.
- 793 Kefauver, S. C., Filella, I., and Peñuelas, J.: Remote Sensing of Atmospheric Biogenic Volatile
794 Organic Compounds (BVOCs) via Satellite-Based Formaldehyde Vertical Column Assessments,
795 *Int. J. Remote Sens.*, 35, 7519-7542, <https://doi.org/10.1080/01431161.2014.968690>, 2014.
- 796 Kim, K.-H., Jahan, S. A., and Lee, J.-T.: Exposure to Formaldehyde and Its Potential Human
797 Health Hazards, *J. Environ. Sci. Health C*, 29, 277-299,
798 <https://doi.org/10.1080/10590501.2011.629972>, 2011.
- 799 Koch, D. M., Khieu, N. H., and Peslherbe, G. H.: Ab Initio Studies of the Glyoxal Unimolecular
800 Dissociation Pathways, *J. Phys. Chem. A*, 105, 3598-3604, <https://doi.org/10.1021/jp0039013>,
801 2001.
- 802 Lacko, M., Piel, F., Mauracher, A., and Španěl, P.: Chemical Ionization of Glyoxal and
803 Formaldehyde with H₃O⁺ Ions using SIFT-MS Under Variable System Humidity, *Phys. Chem.
804 Chem. Phys.*, 22, 10170-10178, <https://doi.org/10.1039/D0CP00297F>, 2020.
- 805 Langer, S., Bekö, G., Bloom, E., Widheden, A., and Ekberg, L.: Indoor air quality in passive and
806 conventional new houses in Sweden, *Build. Environ.*, 93, 92-100,
807 <https://doi.org/10.1016/j.buildenv.2015.02.004>, 2015.
- 808 Lee, M., Heikes, B. G., Jacob, D. J., Sachse, G., and Anderson, B.: Hydrogen Peroxide,
809 Organic Hydroperoxide, and Formaldehyde as Primary Pollutants from Biomass Burning, *J.
810 Geophys. Res. Atmos.*, 102, 1301-1309, <https://doi.org/10.1029/96JD01709>, 1997.
- 811 Li, Z., Schwier, A. N., Sareen, N., and McNeill, V. F.: Reactive Processing of Formaldehyde and
812 Acetaldehyde in Aqueous Aerosol Mimics: Surface Tension Depression and Secondary Organic
813 Products, *Atmos. Chem. Phys.*, 11, 11617-11629, <https://doi.org/10.5194/acp-11-11617-2011>,
814 2011.



- 815 Liggio, J., Li, S.-M., and McLaren, R.: Reactive Uptake of Glyoxal by Particulate Matter, *J.*
816 *Geophys. Res. Atmos.*, 110, <https://doi.org/10.1029/2004JD005113>, 2005.
- 817 Liu, J., Li, X., Yang, Y., Wang, H., Wu, Y., Lu, X., Chen, M., Hu, J., Fan, X., Zeng, L., and
818 Zhang, Y.: An IBBCEAS System for Atmospheric Measurements of Glyoxal and Methylglyoxal
819 in the Presence of High NO₂ Concentrations, *Atmos. Meas. Tech.*, 12, 4439-4453,
820 <https://doi.org/10.5194/amt-12-4439-2019>, 2019.
- 821 Liu, W., Zhang, J., Zhang, L., Turpin, B. J., Weisel, C. P., Morandi, M. T., Stock, T. H., Colome,
822 S., and Korn, L. R.: Estimating contributions of indoor and outdoor sources to indoor carbonyl
823 concentrations in three urban areas of the United States, *Atmos. Environ.*, 40, 2202-2214,
824 <https://doi.org/10.1016/j.atmosenv.2005.12.005>, 2006.
- 825 Lu, X.-W., Jiang, L.-X., Liu, J., Yang, Y., Liu, Q.-Y., Ren, Y., Li, X., and He, S.-G.: Sensitive
826 Detection of Gas-Phase Glyoxal by Electron Attachment Reaction Ionization Mass
827 Spectrometry, *Anal. Chem.*, 91, 12688-12695, <https://doi.org/10.1021/acs.analchem.9b02029>,
828 2019.
- 829 Luecken, D. J., Hutzell, W. T., Strum, M. L., and Pouliot, G. A.: Regional Sources of
830 Atmospheric Formaldehyde and Acetaldehyde, and Implications for Atmospheric Modeling,
831 *Atmos. Environ.*, 47, 477-490, <https://doi.org/10.1016/j.atmosenv.2011.10.005>, 2012.
- 832 Mahajan, A. S., Prados-Roman, C., Hay, T. D., Lampel, J., Pöhler, D., Großmann, K., Tschritter,
833 J., Frieß, U., Platt, U., Johnston, P., Kreher, K., Wittrock, F., Burrows, J. P., Plane, J. M. C., and
834 Saiz-Lopez, A.: Glyoxal Observations in the Global Marine Boundary Layer, *J. Geophys. Res.*
835 *Atmos.*, 119, 6160-6169, <https://doi.org/10.1002/2013JD021388>, 2014.
- 836 Michel, E., Schoon, N., Amelynck, C., Guimbaud, C., Catoire, V., and Arijis, E.: A Selected Ion
837 Flow Tube Study of the Reactions of H₃O⁺, NO⁺ and O₂⁺ with Methyl Vinyl Ketone and Some
838 Atmospherically Important Aldehydes, *Int. J. Mass Spectrom.*, 244, 50-59,
839 <https://doi.org/10.1016/j.ijms.2005.04.005>, 2005.
- 840 Midey, A. J., Arnold, S. T., and Viggiano, A. A.: Reactions of H₃O⁺(H₂O)_n with Formaldehyde
841 and Acetaldehyde, *J. Phys. Chem. A.*, 104, 2706-2709, <https://doi.org/10.1021/jp993797t>, 2000.
- 842 Myriokefalitakis, S., Vrekoussis, M., Tsigaridis, K., Wittrock, F., Richter, A., Brühl, C., Volkamer,
843 R., Burrows, J. P., and Kanakidou, M.: The influence of natural and anthropogenic secondary
844 sources on the glyoxal global distribution, *Atmos. Chem. Phys.*, 8, 4965-4981,
845 <https://doi.org/10.5194/acp-8-4965-2008>, 2008.
- 846 Osseiran, N., Romanias, M. N., Gaudion, V., Angelaki, M. E., Papadimitriou, V. C., Tomas, A.,
847 Coddeville, P., and Thevenet, F.: Development and Validation of a Thermally Regulated
848 Atmospheric Simulation Chamber (THALAMOS): A Versatile Tool to Simulate Atmospheric
849 Processes, *J. Environ. Sci.*, 95, 141-154, <https://doi.org/10.1016/j.jes.2020.03.036>, 2020.
- 850 Rossignol, S., Aregahegn, K. Z., Tinel, L., Fine, L., Nozière, B., and George, C.: Glyoxal
851 Induced Atmospheric Photosensitized Chemistry Leading to Organic Aerosol Growth, *Environ.*
852 *Sci. Technol.*, 48, 3218-3227, <https://doi.org/10.1021/es405581g>, 2014.
- 853 Saito, K., Kakumoto, T., and Murakami, I.: Thermal Unimolecular Decomposition of Glyoxal, *J.*
854 *Phys. Chem.*, 88, 1182-1187, <https://doi.org/10.1021/j150650a033>, 1984.
- 855 Salter, R. J., Blitz, M. A., Heard, D. E., Kovács, T., Pilling, M. J., Rickard, A. R., and Seakins, P.
856 W.: Quantum yields for the photolysis of glyoxal below 350 nm and parameterisations for its
857 photolysis rate in the troposphere, *Phys. Chem. Chem. Phys.*, 15, 4984-4994,
858 <https://doi.org/10.1039/C3CP43597K>, 2013.
- 859 Salthammer, T.: Formaldehyde Sources, Formaldehyde Concentrations and Air Exchange
860 Rates in European Housings, *Build. Environ.*, 150, 219-232,
861 <https://doi.org/10.1016/j.buildenv.2018.12.042>, 2019.
- 862 Sinreich, R., Coburn, S., Dix, B., and Volkamer, R.: Ship-Based Detection of Glyoxal Over the
863 Remote Tropical Pacific Ocean, *Atmos. Chem. Phys.*, 10, 11359-11371,
864 <https://doi.org/10.5194/acp-10-11359-2010>, 2010.



- 865 Smith, D. and Adams, N. G.: The Selected Ion Flow Tube (Sift): Studies of Ion-Neutral
866 Reactions, in: *Adv. At. Mol. Phys.*, edited by: Bates, D., and Bederson, B., Academic Press, 1-
867 49, [https://doi.org/10.1016/S0065-2199\(08\)60229-8](https://doi.org/10.1016/S0065-2199(08)60229-8), 1988.
- 868 Smith, D. and Španěl, P.: Selected Ion Flow Tube Mass Spectrometry (SIFT-MS) for On-line
869 Trace Gas Analysis, *Mass Spectrom. Rev.*, 24, 661-700, <https://doi.org/10.1002/mas.20033>,
870 2005.
- 871 Španěl, P. and Smith, D.: Selected Ion Flow Tube: a Technique for Quantitative Trace Gas
872 Analysis of Air and Breath, *Med. Biol. Eng. Comput.*, 34, 409-419,
873 <https://doi.org/10.1007/BF02523843>, 1996.
- 874 Španěl, P. and Smith, D.: Quantitative Selected Ion Flow Tube Mass Spectrometry: The
875 Influence of Ionic Diffusion and Mass Discrimination, *J. Am. Soc. Mass Spectrom.*, 12, 863-872,
876 <https://doi.org/10.1021/jasms.8b01653>, 2001.
- 877 Stönnner, C., Derstroff, B., Klüpfel, T., Crowley, J. N., and Williams, J.: Glyoxal Measurement
878 with a Proton Transfer Reaction Time of Flight Mass Spectrometer (PTR-TOF-MS):
879 Characterization and Calibration, *J. Mass Spectrom.*, 52, 30-35,
880 <https://doi.org/10.1002/jms.3893>, 2017.
- 881 Thalman, R., Baeza-Romero, M. T., Ball, S. M., Borrás, E., Daniels, M. J. S., Goodall, I. C. A.,
882 Henry, S. B., Karl, T., Keutsch, F. N., Kim, S., Mak, J., Monks, P. S., Muñoz, A., Orlando, J.,
883 Peppe, S., Rickard, A. R., Ródenas, M., Sánchez, P., Seco, R., Su, L., Tyndall, G., Vázquez,
884 M., Vera, T., Waxman, E., and Volkamer, R.: Instrument Intercomparison of Glyoxal, Methyl
885 Glyoxal and NO₂ Under Simulated Atmospheric Conditions, *Atmos. Meas. Tech.*, 8, 1835-1862,
886 <https://doi.org/10.5194/amt-8-1835-2015>, 2015.
- 887 Thevenet, F., Verrielle, M., Harb, P., Thlajeh, S., Brun, R., Nicolas, M., and Angulo-Milhem, S.:
888 The indoor fate of terpenes: Quantification of the limonene uptake by materials, *Build. Environ.*,
889 188, 107433, <https://doi.org/10.1016/j.buildenv.2020.107433>, 2021.
- 890 Vlasenko, A., Macdonald, A. M., Sjostedt, S. J., and Abbatt, J. P. D.: Formaldehyde
891 Measurements by Proton Transfer Reaction – Mass Spectrometry (PTR-MS): Correction for
892 Humidity Effects, *Atmos. Meas. Tech.*, 3, 1055-1062, <https://doi.org/10.5194/amt-3-1055-2010>,
893 2010.
- 894 Volkamer, R., Spietz, P., Burrows, J., and Platt, U.: High-Resolution Absorption Cross-Section of
895 Glyoxal in the UV–vis and IR Spectral Ranges, *J. Photochem. Photobiol. A*, 172, 35-46,
896 <https://doi.org/10.1016/j.jphotochem.2004.11.011>, 2005.
- 897 Volkamer, R., San Martini, F., Molina, L. T., Salcedo, D., Jimenez, J. L., and Molina, M. J.: A
898 Missing Sink for Gas-Phase Glyoxal in Mexico City: Formation of Secondary Organic Aerosol,
899 *Geophys. Res. Lett.*, 34, <https://doi.org/10.1029/2007GL030752>, 2007.
- 900 Warneke, C., Veres, P., Holloway, J. S., Stutz, J., Tsai, C., Alvarez, S., Rappenglueck, B.,
901 Fehsenfeld, F. C., Graus, M., Gilman, J. B., and de Gouw, J. A.: Airborne Formaldehyde
902 Measurements Using PTR-MS: Calibration, Humidity Dependence, Inter-Comparison and Initial
903 Results, *Atmos. Meas. Tech.*, 4, 2345-2358, <https://doi.org/10.5194/amt-4-2345-2011>, 2011.
- 904 Winkowski, M. and Stacewicz, T.: Optical Detection of Formaldehyde in Air in the 3.6 μm
905 Range, *Biomed. Opt. Express*, 11, 7019-7031, <https://doi.org/10.1364/BOE.405384>, 2020.
- 906 Wisthaler, A., Apel, E. C., Bossmeyer, J., Hansel, A., Junkermann, W., Koppmann, R., Meier,
907 R., Müller, K., Solomon, S. J., Steinbrecher, R., Tillmann, R., and Brauers, T.: Technical Note:
908 Intercomparison of Formaldehyde Measurements at the Atmosphere Simulation Chamber
909 SAPHIR, *Atmos. Chem. Phys.*, 8, 2189-2200, <https://doi.org/10.5194/acp-8-2189-2008>, 2008.
- 910 Wróblewski, T., Ziemczonek, L., Alhasan, A. M., and Karwasz, G. P.: Ab Initio and Density
911 Functional Theory Calculations of Proton Affinities for Volatile Organic Compounds, *Eur. Phys. J. Spec. Top.*, 144, 191-195, <https://doi.org/10.1140/epjst/e2007-00126-7>, 2007.
- 912 Xiao, Y., Jacob, D. J., and Turquety, S.: Atmospheric Acetylene and its Relationship with CO as
913 an Indicator of Air Mass Age, *J. Geophys. Res. Atmos.*, 112,
914 <https://doi.org/10.1029/2006JD008268>, 2007.



916 Yuan, B., Koss, A. R., Warneke, C., Coggon, M., Sekimoto, K., and de Gouw, J. A.: Proton-
917 Transfer-Reaction Mass Spectrometry: Applications in Atmospheric Sciences, *Chem. Rev.*, 117,
918 13187-13229, <https://doi.org/10.1021/acs.chemrev.7b00325>, 2017.
919
920